Mon. Not. R. Astron. Soc. **000**, 1–17 (2014) Printed 4 September 2014 (MN LaTeX style file v2.2)

ISIMA Report: Analytic Model of a Star Cluster that Includes Potential Escapers

Kathryne J. Daniel[1⋆⋆†], Douglas Heggie[2] and Anna Lisa Varri[2]

[1] *Johns Hopkins University, Department of Physics & Astronomy, Baltimore, MD 21218, USA*

[2] *University of Edinburgh, School of Mathematics, Edinburgh EH9 3JZ, U.K.*

In original form 4 September 2014

ABSTRACT

A "potential escaper" is a cluster star that has orbital energy greater than the escape energy, and yet, is in a stable orbit. Analytic models of stellar clusters typically have a truncation energy that explicitly excludes these high energy stars. The aim of this study is to build a self-consistent model that includes potential escapers. We present our initial exploration into predicting the orbital stability for potential escapers in terms of approximate integrals of motion. As a first approximation, we assume a constant distribution function and are able to write an expression for the associated density using the region of stability to define the limits of integration for the 0th order moment. In future work we will numerically calculate a self-consistent model that includes potential escapers.

1 INTRODUCTION

Globular clusters are well approximated as spherical, single-population, stellar systems, making them an excellent laboratory for testing for our understanding of simple N-body systems. With such a simple system, it might be expected that a star with a velocity greater than the escape speed will not remain in a stable orbit about the system. Nonetheless, there is evidence for a population of stars, called "potential escapers", that do exactly this. It is the aim of this work to further understand the orbits of this population and to build a "snapshot" model that includes them.

A "snapshot" model is a time-independent model that aims to describe the observed and simulated properties of globular clusters. Such a model is defined by a distribution

function in phase space (f). The fundamental structural and kinematical properties of the cluster can be derived as associated moments in velocity space, with the zeroth, first and second order moments corresponding to the density (ρ), mean velocity vector and velocity dispersion tensor (σ), respectively (see §2).

Several rather successful models have been proposed that have $f = f(E)$ (e.g. Woolley & Dickens 1961; King 1966; Wilson 1975), where $f = 0$ for energies greater than some critical value. The motivation for an energy truncation arises from the following argument. A typical globular cluster is in orbit about a host galaxy. As such, it is natural to consider cluster dynamics in a frame that rotates with the cluster about the galactic center, and throughout this paper we assume that the orbit is circular. The potential in the rotating frame is called the effective potential (Φ_{eff}), and it includes the resulting centrifugal term. The effective potential has two saddle points which are located in a radial line from the galactic center through the center of the cluster, and are at a distance r_J on either side of the cluster. This radial peak in Φ_{eff} can be used to define a critical energy, E_{crit}.[1] A star with energy (in the rotating frame) above the critical energy ($E \geq E_{crit}$) would, naively, not be bound to the cluster. We refer henceforth to such stars inside the cluster as "potential escapers"

To zeroth order, models with $f = f(E)$ and a truncation at $E \geq E_{crit}$ give a good description of observed and N-body data (see McLaughlin & van der Marel 2005, for a detailed discussion). However, there is evidence that potential escapers may significantly contribute to the kinematics and structure of globular clusters. Clusters may have a surface density distribution that is enhanced near the tidal radius as compared to a standard King model (King 1966). This phenomenon has come to be known as "extra-tidal light" (Harris et al. 2002). Of course, the choice of the energy truncation prescription in the definition of the distribution function affects the structural and kinematical properties of the resulting configurations, especially in the outer parts (see Davoust 1977). Smoother truncation prescriptions, such as in Wilson (1975) models, generally produce models with extended haloes, therefore these equilibria are often more successful than King (1966) models in reproducing the surface brightness profiles of Galactic globular clusters in the proximity of the truncation radius. But, extra-tidal lights could also be attributable to a population of potential escapers. The latter view is supported by N-body simulations, which show unbound stars inside the tidal

[1] Note that this is energy in a rotating frame.

radius that significantly enhance the velocity dispersion (e.g. Küpper et al. 2010). Observations of high-energy stars (e.g. Gunn & Griffin 1979; Meylan et al. 1991; Lützgendorf et al. 2012) within the tidal radius give additional evidence for the very stars that presumably contribute to the enhanced velocity dispersion and surface density profiles approaching the tidal radius.

There is, therefore, a need for a model that can successfully describe the presence of stable orbits at $E \geq E_{crit}$. In §2, we give a brief description of the process of building a snapshot model. In §3 we outline the relevant analytic background studies of potential excapers. In §4, we describe our exploration into the important manifold identifying stable orbits for stars with $E \geq E_{crit}$. We make a first attempt at calculating a density distribution in §5. In §6, we discuss our goals for future work on this topic, and in §7 we give a summary of our findings.

2 HOW TO BUILD A "SNAPSHOT" MODEL

The first step toward building a successful snapshot model is to construct a physically motivated distribution function, f, that is a function of some integrals of motion. The prescribed distribution function must satisfy the collisionless Boltzmann equation,

$$\frac{\partial f}{\partial t} + \mathbf{v} \cdot \frac{\partial f}{\partial \mathbf{x}} - \frac{\partial \Phi}{\partial \mathbf{x}} \cdot \frac{\partial f}{\partial \mathbf{v}} = 0, \tag{1}$$

where $\mathbf{x}$ and $\mathbf{v}$ are the coordinate and velocity vectors, and Φ is the underlying potential. As we are interested only in a time-independent model, the first term of eqn. 1 is neglected.

One can determine the associated number density for the globular cluster by taking the 0th moment of f,

$$\rho(\mathbf{x}) = \int f(\mathbf{x}, \mathbf{v}) d^3\mathbf{v}. \tag{2}$$

The self-consistent potential can be calculated via the Poisson's equation,

$$\nabla^2 \Phi = 4\pi G \rho(\mathbf{x}), \tag{3}$$

to get a complete density-potential pair.

A convenient approach to the solution of the Poisson's equation, especially in the case of non-spherical, anisotropic models, is often based on an iteration method, starting from a seed solution (i.e., an initial guess) for the potential Φ (e.g., Prendergast & Tomer 1970). Higher order moments of the distribution function in velocity space define the mean veocity

vector,

$$\langle \mathbf{v}_i \rangle = \frac{1}{\rho(\mathbf{x},t)} \int \mathbf{v}_i \, f(\mathbf{x},\mathbf{v}) \, d^3\mathbf{v}, \tag{4}$$

and the velocity dispersion tensor,

$$\sigma_{ij}^2 = \frac{1}{\rho} \int (v_i - < v >_i)(v_j - < v >_j) \, f(\mathbf{x},\mathbf{v}) d^3\mathbf{v} \tag{5}$$

The velocity dispersion and moments of f should well describe the kinematic and structural properties of observed and simulated globular clusters.

3 IDENTIFYING POTENTIAL ESCAPERS

In order to construct a distribution function that includes the phase space contribution of potential escapers, one must identify stable orbits for these stars in terms of integrals of motion. Fortunately, Henon (1969, 1970) identified two relevant orbital families during his exploration of the restricted 3-body problem in the 2D Hill's approximation. Henon named these families "f-orbits", which are stable, periodic orbits, and "$g3$-orbits", which are marginally stable to unstable, periodic orbits. We will discuss these in more detail in §3.2.

3.1 Defining a coordinate system

For the remainder of this article, it will be convenient to adopt the same coordinate system as did Henon (1969, 1970), where the origin is placed at the center of the globular cluster and is corotating with it. The Cartesian coordinate $\hat{x}$ points radially away from the galactic center, and $\hat{y}$ points in the direction of rotation about the galactic center. For simplicity, a radial coordinate is defined as,

$$r = (x^2 + y^2)^{1/2}. \tag{6}$$

Henon (1969) writes the 2D equations of motion as,

$$\ddot{x} = 2\dot{y} + 3x - \frac{x}{r^3}, \tag{7}$$

and

$$\ddot{y} = -2\dot{x} - \frac{y}{r^3}. \tag{8}$$

Note that if we apply this system the Jacobi integral is expressed in generalized coordinates as,

$$E = \frac{1}{2}\dot{\mathbf{x}}^2 + \Phi_{eff}, \tag{9}$$

where Φ_{eff} is the effective potential

$$\Phi_{eff} = \Phi(\mathbf{x}) + |\Omega_c \times \mathbf{x}|^2, \tag{10}$$

and Ω_c is the orbital angular velocity of the cluster about the galactic center. In the 2D Hill's approximation, Henon (1969, 1970) defines an integral of motion,

$$\Gamma = -2E, \tag{11}$$

which is expressed in our chosen coordinate system as,

$$\Gamma = 3x^2 + \frac{2}{r} - \dot{x}^2 - \dot{y}^2. \tag{12}$$

We extend our analysis to include the third dimension, so that we can explore the full 6D phase space. The $\hat{z}$ component is perpendicular to the $x-y$ plane. The radial coordinate is therefore,

$$r = (x^2 + y^2 + z^2)^{1/2}, \tag{13}$$

and the energy integral of motion becomes,

$$\Gamma = 3x^2 + \frac{2}{r} - z^2 - \dot{x}^2 - \dot{y}^2 - \dot{z}^2. \tag{14}$$

We also derive the equation of motion in the vertical direction to be,

$$\ddot{z} = -z\left(1 + \frac{1}{r^3}\right). \tag{15}$$

3.2 f and $g3$ orbital families

For the reader's convenience, figure 1 shows a re-print of figure 12 from Henon (1970). The horizontal axis shows the energy integral of motion, Γ, in Henon's 2D version. The vertical axis shows the radial distance, x, from the center of the globular cluster. The horizontal hashed regions are "forbidden" in the sense that their surfaces mark the zero velocity curves of the effective potential. A star with $\Gamma < \Gamma_J \equiv 3^{4/3} \simeq 4.33$, will have energy greater than the critical energy. Initial conditions for the f- and $g3$-orbital families, with initial velocities in the $\hat{y}$-direction, are shown by lines marked "f" and "g3". Vertically hashed regions are regions of stability, in the sense that a star launched from position x in the hashed region, with $\dot{x} = 0$ and $\dot{y}$ determined by Γ, will have a stable orbit.

We began our identification of potential escapers through an exploratory analysis of the f- and $g3$-orbital families. In figure 2, we show several examples of f-orbits where we have used the initial conditions published in table 3 of Henon (1969).[2] The orbit is shown in dark

[2] We have used a variable-order integrator from the scientic Python integration library (odeint), and tested our orbits to ensure that the fractional change in Γ remains less than 10^{-6}.

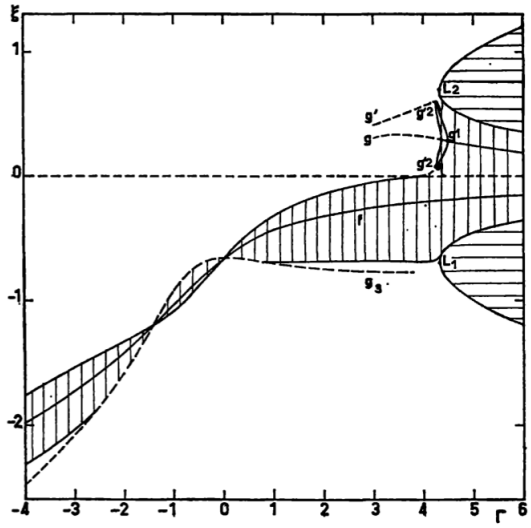

Fig. 12. Summary picture in the (Γ, ξ) plane. Vertical hatching: curve region. Horizontal hatching: forbidden regions. Blank space: escape region. Curves f, g, g', g_3: families of periodic orbits. L_1, L_2: Lagrange points

Figure 1. Figure 12 from Henon (1970). The horizontal axis shows the 2D analogue to the Jacobi integral, Γ, while the vertical axis shows radial distance x from the center of the globular cluster. Lines marked "f" and "g3" give the initial conditions for the f-orbit and $g3$-orbital families.

blue while the tidal radius (r_J) is cyan. f-orbits with low values of Γ appear as approximate epicycles to orbits about the galactic center with guiding center at $x = y = 0$. At high values of Γ, f-orbits appear as approximate circular Keplerian orbits about the cluster. The threshold between "low" and "high" Γ is at $\Gamma \approx 0$, where $\langle x \rangle \approx r_J$. In Henon's analysis, $r_J \equiv 3^{-1/3} \simeq 0.69$. In figure 3, we plot the initial position, x_0, versus the associate Γ for both f-orbits (Henon 1969) and Keplerian orbits. We find that Keplerian orbits are a good approximation to f-orbits when $\Gamma \gtrsim 0$.

A similar analysis to that shown in fig. 2 is shown in figure 4 for the unstable $g3$-orbital family. The initial conditions are taken from table 1 in Henon (1970). Note that while some of these orbits appear stable, we have only integrated them for a single orbital period in fig. 4. Integrations of more than one period show that many of the stars in these orbits are quickly lost as members of the globular cluster.

4 STABILITY OF POTENTIAL ESCAPERS

Identification of f- and $g3$-orbital families from Henon (1969, 1970) are an important first step toward understanding the nature of potential escapers. However, in this study we aim to understand the parameters important to orbital stability when $E > E_{crit}$. It is reasonable to presume that the orbits of potential escapers are filled from high to low Γ (low to high

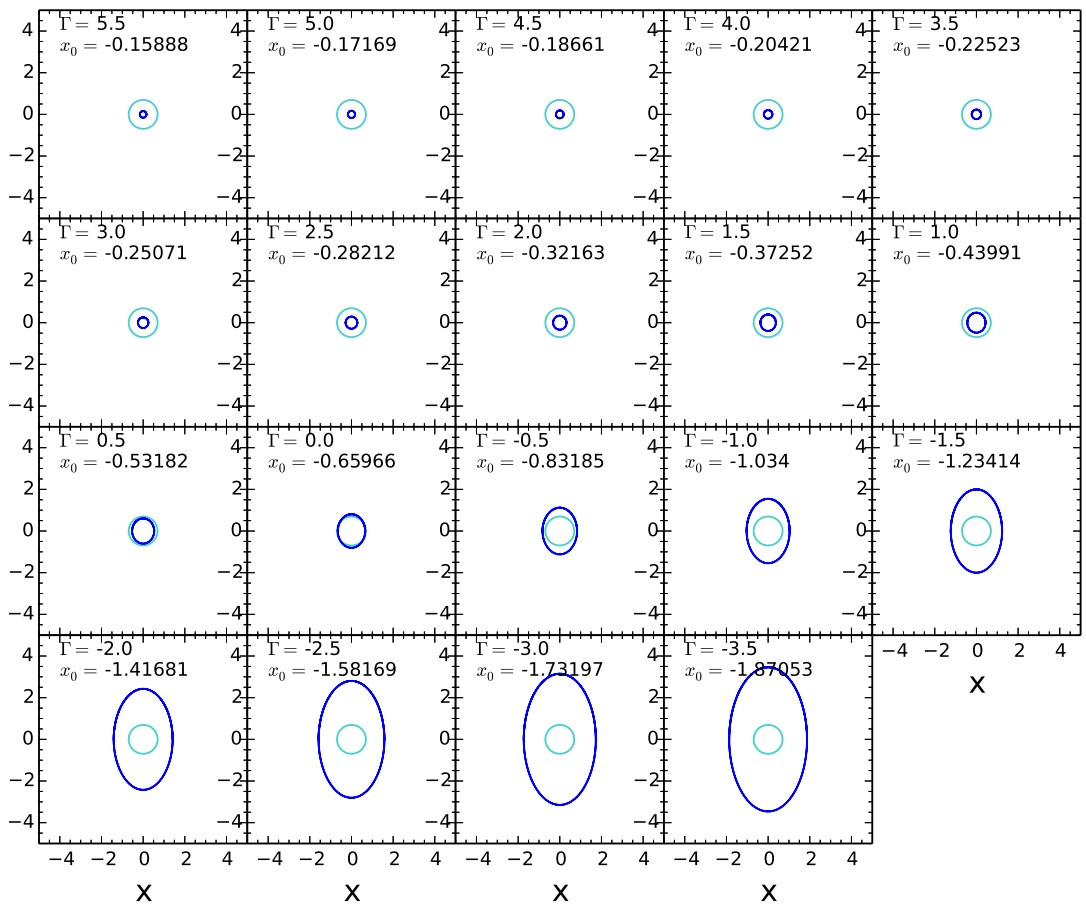

Figure 2. Examples of stable f-orbits with initial conditions from Henon (1969). The associated Γ and initial position, x_0, for each orbit is printed as an inset.

E), as these orbits are likely populated as the cluster relaxes. We therefore limit the current exploration to the region of stability within fig. 1 where the initial radius is within the tidal radius, $|r_0| < r_J$, and $\Gamma > 0$.

Using figure 1 as a guide, we perform an empirical stability analysis. We first explore the orbits in the $x - y$ plane by filling the vertically hashed region of interest in fig. 1. We then extend our analysis to the third dimension.

In figure 5 we show a sample of our stability analysis in the plane. The leftmost column shows $g3$-orbits with $\Gamma > 0$. Each column to the right has an initial position, x_0, that incrementally increases by 0.1 (in Henon units), where Γ is held constant in each row. We integrated each orbit for five orbital periods and then evaluated its stability, where an unstable orbit has an orbital radius that is greater than the tidal radius ($r_{max} > r_J$) at some

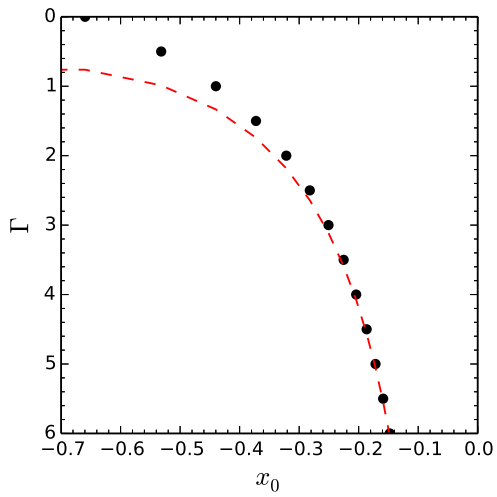

Figure 3. Initial position, x_0, versus the associated Γ for f-orbits. Circles show the data from Henon (1969), and the dashed, red line shows the relationship between x_0 and Γ for a Keplerian orbit. Note that f-orbits are well approximated by the Keplerian orbits for $\Gamma \gtrsim 0$.

time during the integration. We flagged each test orbit as unstable (red background), stable (lavender background), or uncertain (no example shown in fig. 5).

As illustrated in figure 6, we extend our analysis to 3D by perturbing f-orbits with an inclination. The leftmost column shows f-orbits in the plane. Each row has the same initial launch radius and value for Γ, while the inclination (i) of the initial position vector to the $x-y$ plane is incrementally increased by 15° with each column toward the right. The initial velocity is in the $\hat{y}$-direction with amplitude determined by Γ. As expected, stars with $E \gtrsim E_{crit}$ tend to become unstable when $i > 90°$, as these are pro-grade orbits[3].

The stability analysis for fig. 6 has colours with the same meaning as in fig. 5 with the addition of a third flag for uncertain stability (yellow background). Each orbit was also plotted in the $x-z$ and $y-z$ planes, but these are not shown here.

4.1 Stability in a manifold of approximate integrals of motion

For every orbit we evaluated, the value of Γ (the energy integral of motion) is known. The initial amplitude of the total angular momentum, $|\mathbf{L}|$, and the value of its component in the $\hat{z}$-direction, L_z, can be evaluated. Each orbit is launched from $y_0 = 0$ and with $\mathbf{v}_0 = v_0\hat{y} = v_{y,0}$. Therefore, an orbit with a given Γ, radius r, and inclination i, will have $x_0 = r\cos i$ and $z_0 = -r\sin i$. Eqn. 14 can be used to solve for $v_{y,0}$. In this scheme, $|\mathbf{L}| = r\,|v_{y,0}|$ and

[3] Pro-grade orbits will have a Coriolis force away from the cluster.

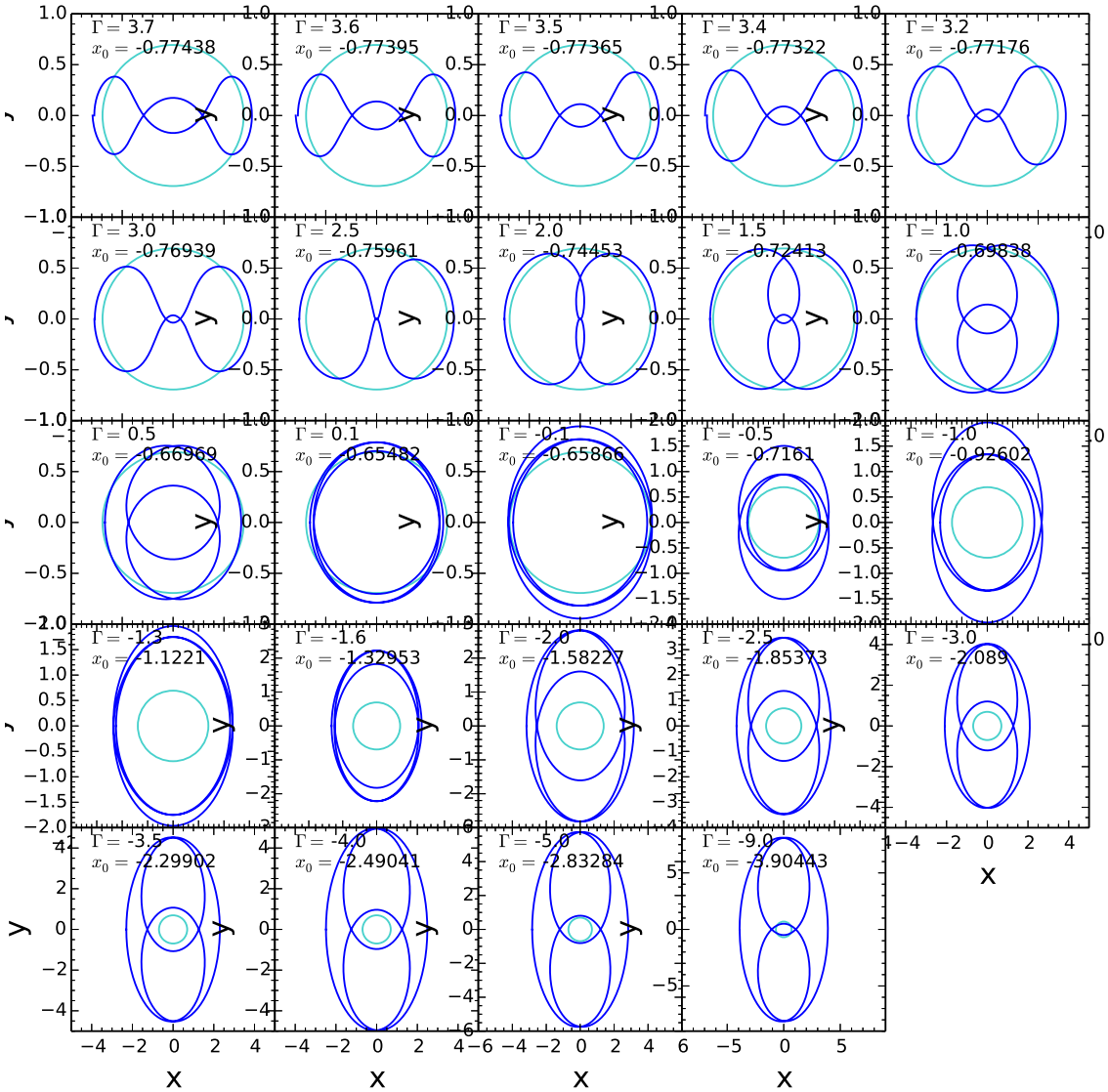

Figure 4. Examples of stable $g3$-orbits with initial conditions from Henon (1970). The associated Γ and initial position, x_0, for each orbit is printed as an inset.

$L_z = x_0\, v_{y,0}$. As long as the orbits of potential escapers (stable orbits) can be treated as perturbations to Keplerian motions, L_z and $|\mathbf{L}|$ can be treated as approximate integrals of motion.

The left panel of fig. 7 shows a scatter plot of L_z vs Γ for each orbit we evaluated for stability. Plus and cross signs are orbits in the $x - y$ plane (two symbols are used for visual differentiation only and have no physical meaning), and circles are for inclined f-orbits. The

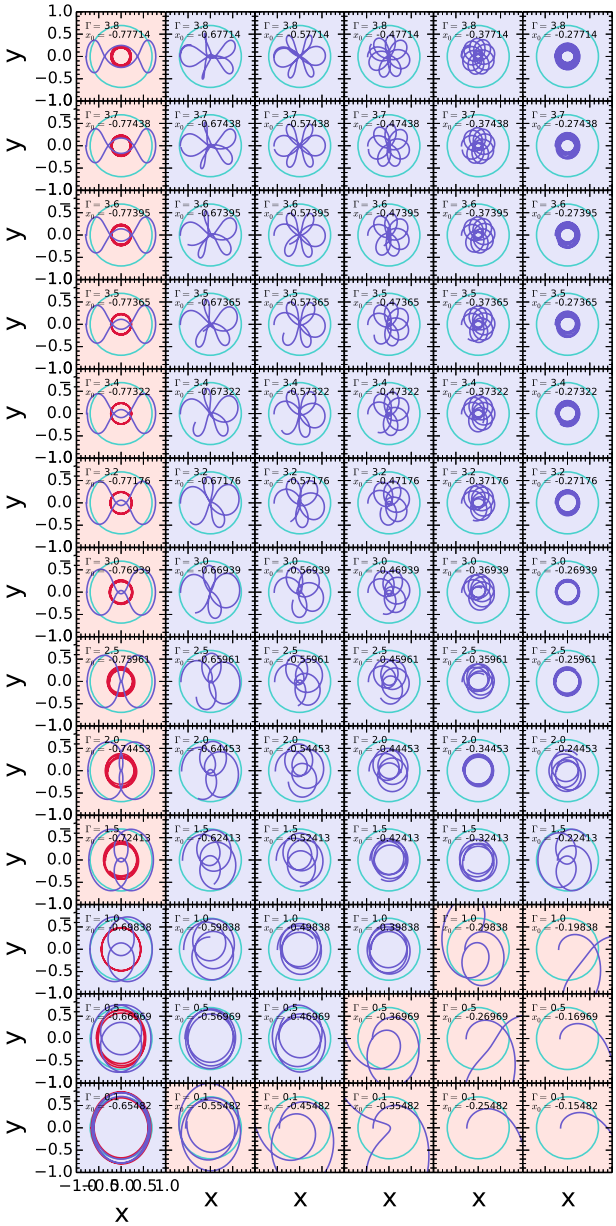

Figure 5. $g3$-orbits with initial conditions from Henon (1970) are in the leftmost column. Γ is held constant in each row, where the value of x_0 is increased by 0.1 (in Henon units) with each step to the right. The associated Γ and initial position, x_0, for each orbit is printed as an inset. The orbital trajectory is plotted in purple. In the leftmost column, the cyan circle shows the tidal radius. For reference, the trajectory of the approximate f-orbit associated with a given Γ (derived from a line of best fit to the Henon data) is plotted in red. Note that some approximated f-orbits are slightly perturbed, and the overlap of their path over several orbital periods appears as a thick, red line. The stability of each orbit is determined empirically, where a red background indicates an unstable orbit and a lavender background indicates stability.

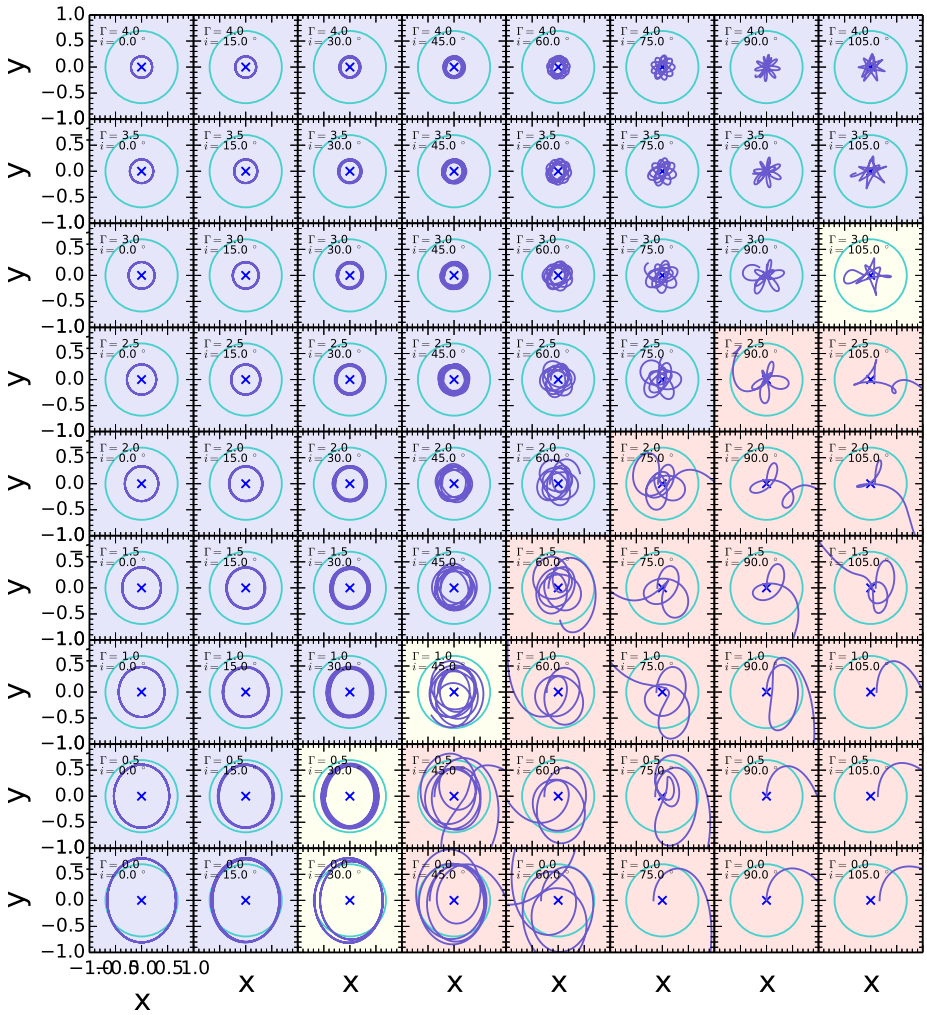

Figure 6. Stable f-orbits with initial conditions from Henon (1969) are in the leftmost column. The initial radius and Γ are held constant in each row, where the inclination of the orbit, i, is increased by $15°$ with each step to the right. The associated Γ and inclination for each orbit is printed in the inset. The orbital trajectory is plotted in purple. The cyan circle shows the tidal radius. The stability of each orbit is determined empirically, where a red background indicates an unstable orbit, a lavender background indicates stability, and a yellow background indicates uncertain stability.

green line marks f-orbits (analogous to the curve for f-orbits in fig. 1). The red line marks the angular momentum for a star of given Γ that is launched in the $x - y$ plane from r_J with velocity in the $\hat{y}$-direction as determined by Γ. We will henceforth call this the lower boundary for L_z, or $L_{z,low}$, as this appears to be a good delimitation for stability. The upper boundary for L_z, or $L_{z,up}$, is shown as a magenta line. This is a line of "best fit", in the sense that we have simply placed a line that roughly separates stable from unstable orbits for $\Gamma < 2.5$. For $\Gamma_J > \Gamma \geq 2.5$, we assume $L_{z,up} = 0$, in order to eliminate pro-grade orbits.

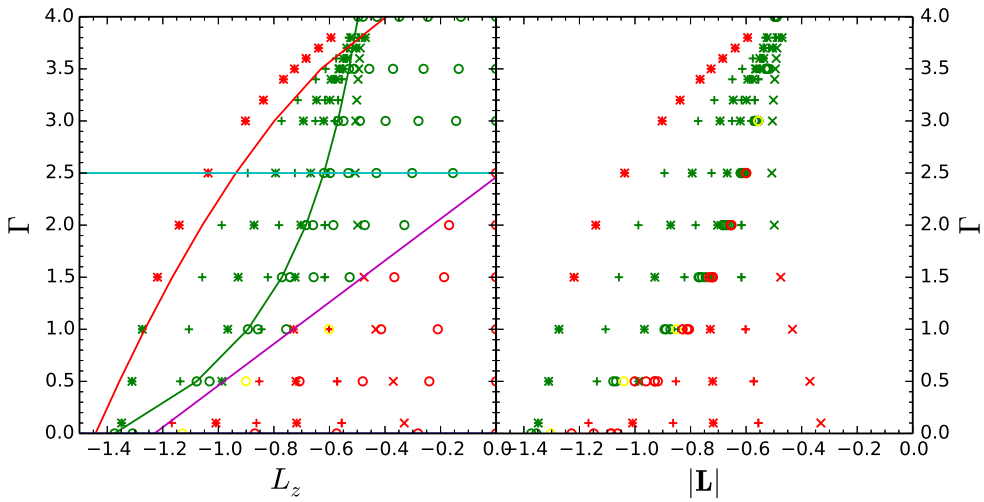

Figure 7. Scatter plots of L_z vs Γ and $|\mathbf{L}|$ vs Γ for all orbits evaluated for stability. Cross and plus symbols indicate orbits in the $x-y$ plane, and circles indicate inclined f-orbits. Colour corresponds to the stability of the orbit (green is stable, red is unstable, yellow is undetermined stability).

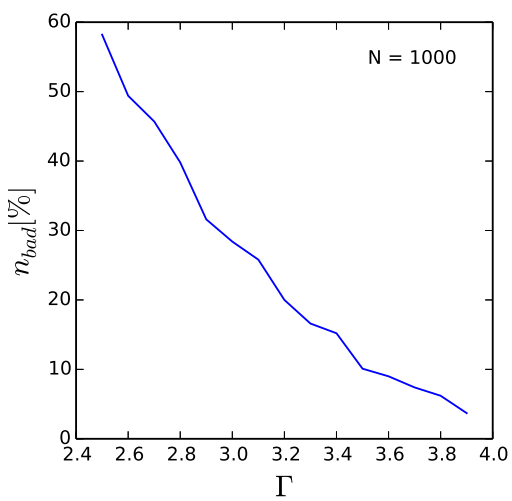

Figure 8. Unstable orbits within the range $2.5 \leq \Gamma \leq 4$ that meet our criterion ($L_{z,low}(\Gamma) < L_z \leq L_{z,up}(\Gamma)$). Should our criterion be viable, the flagged percent (n_{bad}) would be nearly zero for all Γ.

Below, we test the validity of our characterisation of stability as being defined by the region where $L_{z,low}(\Gamma) < L_z \leq L_{z,up}(\Gamma)$.

The right panel of fig. 7 is a scatter plot of $|\mathbf{L}|$ vs Γ where the the colours and symbols have the same meanings as in the left panel. It is tempting to consider the very tight clustering of $|\mathbf{L}|$ at high Γ as an indication of stability. However, the overlap in stable and unstable orbits in this manifold for lower values of Γ renders the evaluation of $|\mathbf{L}|$ to be less useful than L_z given the relatively clean separation of stability in the $L_z - \Gamma$ manifold.

We test our characterisation of orbital stability in the $L_z - \Gamma$ manifold through extensive

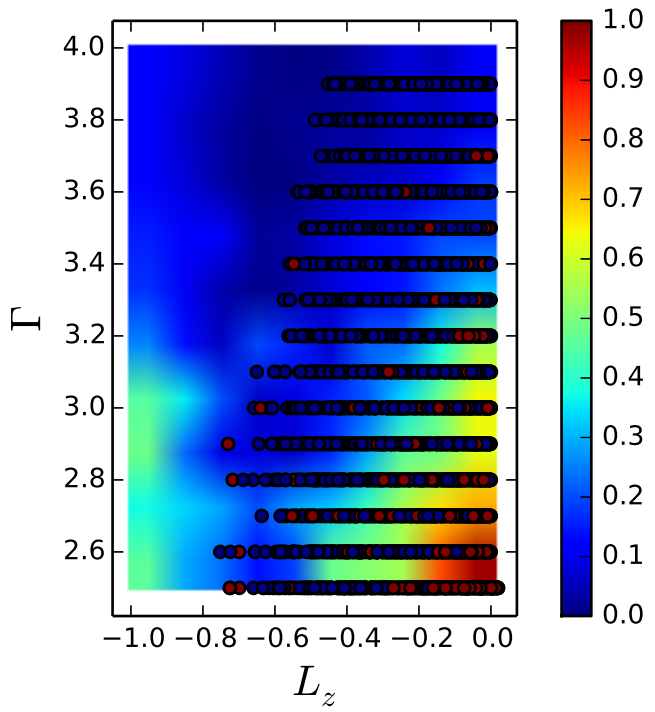

Figure 9. Linearly interpolated heat map of stability for orbits that meet our criterion. Blue indicates a region where our evaluation of stability is correct, where red indicates a poor evaluation of stability. Note that the enhanced region in the lower left may be noise that is amplified by the interpolation, while the region to the lower right makes a clear prediction that our criterion in this region are inadequate.

Monte Carlo simulations. We ran 1000 random realisations of initial conditions for each value of Γ between $2.5 - 4$ in increments of $\Delta\Gamma = 0.1$. For each realisation, we randomly select an amplitude for the initial radius that is less than the tidal radius ($r_0 \leq r_J$), and then randomly select the vector direction of the initial position. Using the value of Γ, we solve for the amplitude of the velocity vector and randomly assign the direction. Orbits with $L_{z,low}(\Gamma) < L_z \leq L_{z,up}(\Gamma)$ are integrated for several orbital periods, while orbits that do not meet this criterion are discarded. Orbits that have $|r| > r_J$ at some point during their integration are flagged as unstable. In principle, should our criteria for stability be well posed, we would have zero flagged orbits in these simulations. Figure 8 shows the percentage of flagged (unstable) orbits as a function of Γ (n_{bad}). The value of n_{bad} increases nearly linearly with decreasing Γ.

We investigate our evaluation of the stability criterion in figure 9. Each realisation of the Monte Carlo simulation is plotted as a circle, where blue signifies a stable orbit and red signifies an unstable (flagged) orbit. A linear interpolation of the scatter plot is shown as a heat map, where blue indicates a region where our evaluation of stability well describes the

data. The enhanced (green) region at $L_z \sim -1$ and $2.5 < \Gamma \lesssim 3.1$ has two explanations. First, this region is close to the boundary of our assumed stable region, and so it may be expected that our stability criterion give a poor prediction for stability. Second, there are very few data points sampled in this region and the linear interpolation, which is implicit in the production of the heat map, is slightly noisy. In the region where L_z approaches zero, and $2.5 < \Gamma \lesssim 3.5$, there is a strong enhancement indicating that our line of "best fit" for $L_{z,up}$ is a poorly evaluated marker of stability.

In future work, we will change $L_{z,up}$ to exclude this region from our evaluation of the region of stability in the $L_z - \Gamma$ manifold with the expectation that the value of n_{bad} will decrease for values of $\Gamma \lesssim 3.5$. For the current study, however, we use $\Gamma = 2.5$ as a lower limit to the region of Γ for which we will evaluate the density of potential escapers.

5 CONSTRUCTION OF THE MODEL

5.1 Choice of the distribution function

For simplicity, we will first consider a model defined by a constant distribution function over the domain set by the manifold identified in the previous section. The construction of models based on more complicated analytical expressions for the distribution function (e.g., lowered Maxwellian distribution functions) will be explored in the near future.

5.2 Density determination

In order to calculate the density associated with the distribution function, it is convenient to use a partition of the phase space in terms of the selected approximated integrals of the motion, Γ and L_z. We can then define meaningful limits of integration within the manifold defining the domain of the distribution function.

The integral over velocity space (eqn. 2) is expressed in cylindrical polar coordinates as $d^3\mathbf{v} = dv_\phi \, dv_R \, dv_z$. We can uniquely describe the same space by defining a new coordinate, $v_\perp = (v_R^2 + v_z^2)^{1/2}$, and an accompanying angle, ψ, that can be integrated over 2π. This transformation gives,

$$\rho(\mathbf{x}) = 2\pi \int v_\perp \, dv_\perp \int dv_\phi \, f. \tag{16}$$

We can further transform the variables of integration into $\Gamma - L_z$ space using eqns. 10-11,

so that the Jacobian,

$$J = \frac{\partial(\Gamma, L_z)}{\partial(v_\perp, v_\phi)} = 2v_\perp R, \tag{17}$$

and,

$$\rho(\mathbf{x}) = \frac{\pi f}{R} \int d\Gamma \int dL_z, \tag{18}$$

where R is the radial cylindrical-polar coordinate.

We use eqns. 9-11 and the relation $L_z = Rv_\phi$, to show that,

$$\Gamma = -2\Phi_{eff} - \dot{\mathbf{x}}^2, \tag{19}$$

and thus expressing Γ in terms of the generalized potential. We can set the limits of integration over $d\Gamma$ via the physically motivated argument that potential escapers have $-\infty < \Gamma \leq \min\{-2\Phi_{eff,J}, -2\Phi_{eff}\}$, where $\Phi_{eff,J}$ is the value of Φ_{eff} evaluated at the saddle point located at $(x, y) = (-r_J, 0)$ in Henon's Cartesian coordinate system.

The limits of integration over dL_z can be expressed in terms of Φ_{eff} by using eqn. 19, to show that $v_\phi = -R(-\Gamma - 2\Phi_{eff})^{1/2}$ when $v_\perp = 0$. From §4.1, the lower limit of integration over dL_z is therefore $\max\{-r_J(-\Gamma - 2\Phi_{eff,J})^{1/2}, -R(-\Gamma - 2\Phi_{eff})^{1/2}\}$. By expressing our line of "best fit" as some function, $F(\Gamma)$, then the upper limit of integration over dL_z is $\min\{0, F(\Gamma)\}$. In terms of the boundary conditions set by this study, the density of potential escapers would be,

$$\rho(\mathbf{x}) = \frac{\pi f}{R} \int_{-\infty}^{\min\{-2\Phi_{eff,J}, -2\Phi_{eff}\}} d\Gamma \int_{\max\{-r_J(-\Gamma-2\Phi_{eff,J})^{1/2}, -R(-\Gamma-2\Phi_{eff})^{1/2}\}}^{\min\{0, F(\Gamma)\}} dL_z. \tag{20}$$

We can further assume that the region of interest in the $\Gamma - \text{Ł}_z$ manifold is populated from high to low values of Γ, and therefore, we set the lower limit of the integral over $d\Gamma$ to some value $\xi \geq 0$. By assigning a value of ξ such that $\min\{0, F(\Gamma)\} = 0$, eqn. 20 becomes,

$$\rho(\mathbf{x}) = \frac{\pi f}{R} \int_{\xi}^{\min\{-2\Phi_{eff,J}, -2\Phi_{eff}\}} d\Gamma \int_{\max\{-r_J(-\Gamma-2\Phi_{eff,J})^{1/2}, -R(-\Gamma-2\Phi_{eff})^{1/2}\}}^{0} dL_z. \tag{21}$$

The integral over dL_z in eqn. 21 is just,

$$\rho(\mathbf{x}) = \frac{\pi f}{R} \int_{\xi}^{\min\{-2\Phi_{eff,J}, -2\Phi_{eff}\}} d\Gamma \min\{r_J(-\Gamma - 2\Phi_{eff,J})^{1/2}, R(-\Gamma - 2\Phi_{eff})^{1/2}\}. \tag{22}$$

One would use the first expression in the integration over $d\Gamma$, (i.e., $r_J(-\Gamma - 2\Phi_{eff,J})^{1/2}$) in the case that,

$$\begin{aligned} r_J(-\Gamma - 2\Phi_{eff,J})^{1/2} &\leq R(-\Gamma - 2\Phi_{eff})^{1/2} \\ \Gamma &\geq \frac{-2\Phi_{eff,J} + 2\Phi_{eff}(R/r_J)^2}{1 - (R/r_J)^2} \end{aligned} \tag{23}$$

It is now possible to attain an approximation of the density once one assumes an underlying potential. A seed prescription for the analytic evaluation of $\rho(\mathbf{x})$, the numerical solution

for the self-consistent potential, and resulting expression for the distribution function will be addressed in the near future.

6 FUTURE WORK

As a continuation of this work, we will first need to determine a lower limit for L_z that better describes the region of stability in the $L_z - \Gamma$ manifold. This will enable us to place meaningful limits of integration for our first evaluation of the density (e.g. §5). We will also explore the possibility of a third integral of the motion (e.g., $|\mathbf{L}|$), in the definition of the boundary of the manifold.

As outlined in §2, we will use this initial evaluation of the density to improve our definition of orbits of stable potential escapers and hence the analytical expression of the distribution function, f, as a function of the 6D phase-space in a self-consistent potential. We will continue to refine $f(\mathbf{x}, \mathbf{v})$ with evaluations of higher moments of the distribution function (eqns. 4 & 5) and their fit to N-body simulations and observational data.

7 SUMMARY

This report describes our initial exploration into building a "snapshot" model that includes potential escapers in a star cluster. A continuation of this work will be published in the near future.

We first identified the f- and $g3$-type orbital families (Henon 1969, 1970), which have $E \geq E_{crit}$. We found that the motions of a star in an f-type orbit are well described by Keplerian motion when the star is within the tidal radius.

Under the assumption that the motions of potential escapers can be treated as perturbations to Keplerian orbits, we identify three integrals of motion: Γ, $|\mathbf{L}|$, and L_z, corresponding to the energy, total angular momentum and the $\hat{z}$ component of the angular momentum. Via an empirical analysis of orbital stability within the space defined by the above integrals of motion, we find the domain within the $\Gamma - L_z$ manifold that constrains orbital stability for stars with $E > E_{crit}$ (i.e., potential escapers).

Our goal is to find a self-consistent model that includes potential escapers. As a first step, we calculate an associated density by expressing the 0th order moment of a constant distribution function in terms of the above identified manifold, with limits of integration defined by the domain that encloses stable orbits.

In future work, we will use our initial calculation for the density to numerically calculate the associated, self-consistent potential. We will iteratively refine our model with evaluations of higher moments of the distribution function, and through their fit to N-body simulations and observational data.

ACKNOWLEDGMENTS

It is a pleasure to thank Mark Geiles, Ben Bar-Or, Filippo Contenta, and Maxwell Tsai for many helpful discussions during the course of this work. This study was initiated during the International Summer-Institute for Modeling in Astrophysics (ISIMA) in 2014, hosted at CITA at the University of Toronto.

REFERENCES

Davoust E., 1977, A&A, 61, 391

Gunn J. E., Griffin R. F., 1979, AJ, 84, 752

Harris W. E., Harris G. L. H., Holland S. T., McLaughlin D. E., 2002, AJ, 124, 1435

Henon M., 1969, A&A, 1, 223

Henon M., 1970, A&A, 9, 24

King I. R., 1966, AJ, 71, 64

Küpper A. H. W., Kroupa P., Baumgardt H., Heggie D. C., 2010, MNRAS, 407, 2241

Lützgendorf N., Gualandris A., Kissler-Patig M., Gebhardt K., Baumgardt H., Noyola E., Kruijssen J. M. D., Jalali B., de Zeeuw P. T., Neumayer N., 2012, A&A, 543, A82

McLaughlin D. E., van der Marel R. P., 2005, ApJS, 161, 304

Meylan G., Dubath P., Mayor M., 1991, ApJ, 383, 587

Prendergast K. H., Tomer E., 1970, AJ, 75, 674

Wilson C. P., 1975, AJ, 80, 175

Woolley R. v. d. R., Dickens R. J., 1961, Royal Greenwich Observatory Bulletins, 42, 291